RSC Advances

ROYAL SOCIETY OF CHEMISTRY

PAPER

View Article Online
View Journal | View Issue



Cite this: *RSC Adv.*, 2026, **16**, 18011

# Facile sonochemical route to sponge-like porous AgCl/malachite for enhanced photocatalytic performance and stability

Hongbo He, * Simin Zhong, Wanting Xiao, Jianhong Jiang, Yijun Guo, Siyao Tan, Shiya He, Midong Shi, Erjun Zhang* and Bin Deng*

Addressing the persistent challenges of photochemical corrosion and poor stability in silver-based photocatalysts, this study proposes a sonochemical synthesis strategy to construct sponge-like porous AgCl/Malachite heterojunction composites. The as-prepared material exhibits outstanding photocatalytic activity and cycling stability toward methyl orange (MO). Under light irradiation, the composite achieves a degradation efficiency of 92.8% within 30 min, with a reaction rate constant of 0.08352 $min^{-1}$, which is 39.4 times higher than that of pure Malachite and 1.9 times greater than pure AgCl. Importantly, the photocatalytic performance shows no significant degradation after five consecutive cycles. The enhanced performance is attributed to the following factors: the formed heterojunction between AgCl and Malachite effectively promotes the separation and transfer of photogenerated charge carriers. The hierarchical porous structure and high specific surface area optimize mass transfer during the reaction and provide abundant active sites. Moreover, the composite architecture significantly suppresses the photochemical corrosion of AgCl. This work not only offers a new approach to mitigating the photochemical corrosion of silver-based materials for developing highly efficient and stable photocatalysts, but also provides a fast and controllable sonochemical route for the scalable synthesis of functional heterojunction materials with potential for industrial production.

Received 12th February 2026
Accepted 28th March 2026

DOI: 10.1039/d6ra01246a

rsc.li/rsc-advances



## 1. Introduction

Water scarcity and aquatic pollution represent severe challenges to the sustainable development of human society. Despite the vast overall volume of water on Earth, the proportion accessible as fresh water for direct human use is extremely limited, accounting for only about 0.26% of the total global water reserves.[1] Concurrently, industrial activities, particularly the textile dyeing and finishing sector, discharge large volumes of complex, bio-recalcitrant organic dye wastewater, further exacerbating the water crisis. Conventional water treatment technologies, including physical, chemical, and biological methods, exhibit significant limitations in treating such effluents: physical adsorption merely transfers pollutants between phases; chemical oxidation often generates harmful by-products; and biological degradation is constrained by microbial sensitivity, substrate specificity, and lengthy treatment cycles.[2,3] Consequently, the development of efficient, green, and broadly applicable water treatment technologies has become an urgent scientific priority.

Semiconductor photocatalysis is regarded as a highly promising green technology for water remediation due to its ability to directly utilize solar energy and completely mineralize organic pollutants into harmless small molecules such as $CO_2$ and $H_2O$ under mild conditions.[4–6] The core process involves photoexcitation of the catalyst to generate electron–hole pairs, which subsequently yield highly reactive radical species (*e.g.*, $^{\bullet}OH$ and $^{\bullet}O_2^-$) capable of non-selective deep oxidation of pollutants.[7–9] However, photocatalytic efficiency is fundamentally limited by the rapid recombination of photogenerated charge carriers. Therefore, designing and fabricating high-performance photocatalysts that can effectively promote charge separation is key to advancing this technology toward practical application. Among various photocatalytic materials, silver halides (AgX, X = Cl, Br, I) have attracted considerable attention due to their unique photosensitive properties and visible-light response potential.[10–12] In particular, silver chloride (AgCl)-based materials have been extensively studied. For instance, Abdel-Hafeez *et al.* [13] achieved the green synthesis of Ag/AgCl nanocomposites using plant extracts and demonstrated their potential in dye degradation. Wang *et al.*[14] constructed core–shell $Ag_2MoO_4$@AgCl heterojunctions, which significantly enhanced charge carrier separation efficiency and antibiotic degradation performance. Our previous study also showed that loading Ag/AgCl nanoparticles onto a diatomite/g-

*Hunan Provincial Key Laboratory of Xiangnan Rare-Precious Metals Compounds and Applications, College of Chemistry and Environmental Science, Xiangnan University, Chenzhou 423000, P. R. China. E-mail: hehb5@mail2.sysu.edu.cn; zhz.219@163.com; ddhbyjs@126.com*

$C_3N_4$ composite support effectively suppressed agglomeration and promoted interfacial charge transfer, thereby improving Cr(VI) reduction activity.[15] Nonetheless, AgCl-based materials commonly suffer from severe photo-corrosion, wherein $Ag^+$ is easily reduced to $Ag^0$ or the AgCl structure itself deteriorates under illumination,[16,17] leading to rapid degradation of catalytic activity. This remains a critical bottleneck hindering their practical application.

To overcome this drawback, constructing a heterojunction with another semiconductor possessing matched band structures, structural stability, and low cost is considered an effective strategy to simultaneously inhibit photo-corrosion and enhance charge separation efficiency.[18,19] Malachite ($Cu_2(OH)_2CO_3$), a natural mineral semiconductor, exhibits inherent photocatalytic potential due to its unique layered structure, abundant surface hydroxyl groups, and the multivalent character of copper ions. These properties also make it an excellent stabilizing support or co-catalyst.[20] Combining AgCl with malachite is expected to create a closely coupled heterojunction interface. This architecture could suppress AgCl photo-corrosion while establishing an efficient charge transfer channel through band alignment synergy, thereby achieving concurrent improvements in performance and stability.

Based on this rationale, this study innovatively proposes a rapid and controllable sonochemical method to fabricate a novel sponge-like porous AgCl/Malachite heterojunction composite. The design aims to achieve three primary objectives: (1) to drive the efficient spatial separation of photogenerated charge carriers through the formation of an intimate heterojunction interface between AgCl and Malachite, while utilizing the stable chemical environment of Malachite to inhibit AgCl photo-corrosion; (2) to optimize reaction mass transfer and provide abundant active sites by leveraging the multi-level pore structure and high specific surface area induced by the sonochemical synthesis; (3) to comprehensively enhance the visible-light catalytic activity and cycling stability of the material by synergizing plasmonic resonance effects with heterojunction advantages. This work not only provides a new approach for developing long-lived, high-performance silver-based photocatalysts but also offers a valuable reference for the design and controllable synthesis of functional heterojunction materials through its fast and controllable synthetic strategy.

## 2. Experimental section

### 2.1. Synthesis of AgCl/Malachite

First, copper(II) chloride dihydrate ($CuCl_2 \cdot 2H_2O$, 10 mmol) was dissolved in 15 mL of deionized water under stirring until completely dissolved, denoted as Solution A. Subsequently, anhydrous sodium carbonate ($Na_2CO_3$, 10 mmol) was dissolved in 15 mL of deionized water to obtain Solution B. Under continuous stirring, Solution B was added dropwise to Solution A, and the resulting mixture was labeled as Suspension C. Next, silver nitrate ($AgNO_3$, 13 mmol) was dissolved in 3 mL of deionized water, denoted as Solution D. Under continuous stirring, Solution D was slowly added dropwise to Suspension C. The reaction was carried out in an ice-water bath with the assistance of ultrasound (LC-UP-400, equipped with a $\Phi$6 horn, Shanghai Lichen Bangxi Technology Co., Ltd) in pulse mode (2 s on, 2 s off, 50% output power) for 20 min. The temperature of the reaction mixture was monitored using a thermocouple and maintained at 2–5 °C throughout the process. The resulting product was collected by centrifugation and washed three times each with deionized water and absolute ethanol. Finally, it was dried in a forced-air drying oven at 60 °C for 12 h to obtain the AgCl/Malachite heterojunction.

### 2.2. Characterization

The physicochemical properties of the as-prepared AgCl/Malachite catalysts were characterized by powder X-ray diffraction (XRD), field-emission scanning electron microscope (SEM), $N_2$ physical adsorption, ultraviolet-visible diffuse reflectance spectra (UV-vis DRS), transient photocurrent response (TPR), electrochemical impedance spectroscopy (EIS). The details of characterizations were given in SI.

### 2.3. Photocatalysis tests

The photocatalytic tests were conducted in a photochemical reactor with a 400 W metal halide lamp ((with a broad emission spectrum covering both UV and visible light, typically 350–450 nm)) as the light source. 15 mg of the sample was added to 40 mL of MO aqueous solution (30 mg $L^{-1}$). The resulting suspension was stirred in the dark for 40 minutes to achieve adsorption–desorption equilibrium prior to light irradiation, while the temperature of the suspension was maintained at approximately 25 °C with cyclic cooling water. Approximately 1.5 mL of the suspension was sampled every 8 min, and the solid was filtered by centrifugation. Finally, the concentration of the MO was analyzed using a UV-vis spectrophotometer at its maximum absorption wavelength. Details regarding the radical capturing and cycle experiments are described in the SI.

## 3. Results and discussion

### 3.1. Characterizations of the catalysts

The crystalline structure of the catalyst was comprehensively characterized *via* X-ray powder diffraction (XRD), with the results illustrated in Fig. 1. For the AgCl sample, distinct diffraction peaks were observed at 27.8°, 32.2°, 46.2°, 54.8°, 57.5°, 67.5°, 74.5°, and 76.8°. These peaks correspond precisely to the (111), (200), (220), (311), (222), (400), (331), and (420) crystal planes of cubic AgCl, as referenced in JCPDS No. 01-085-1355, with lattice parameters $a = b = c = 5.55$ Å and $\alpha = \beta = \gamma = 90°$. In the case of the Malachite sample, characteristic diffraction peaks emerged at 14.8°, 17.6°, 24.1°, 31.2°, and 35.6°. These are indicative of the (020), (120), (220), (20–1), and (240) crystal planes of monoclinic $Cu_2(OH)_2CO_3$, as per JCPDS No. 00-041-1390, featuring lattice parameters $a = 9.50$ Å, $b = 11.94$ Å, $c = 3.25$ Å, $\alpha = 90°$, $\beta = 98.7°$, and $\gamma = 90°$. The XRD pattern of the AgCl/Malachite composite material revealed the presence of characteristic diffraction peaks from both AgCl and Malachite, providing conclusive evidence for the successful

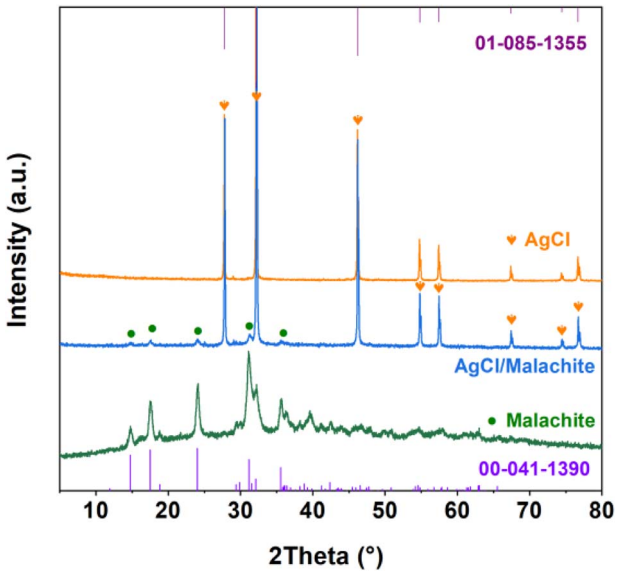


Fig. 1 XRD patterns of AgCl, Malachite and AgCl/Malachite composites.

synthesis of the AgCl/Malachite heterojunction composite *via* the sonochemical method.

The surface morphology and microstructure of the catalysts were characterized by field-emission scanning electron microscopy (FE-SEM), with the results shown in Fig. 2. The Malachite exhibits a typical micron-scale structure composed of agglomerated primary nanoparticles (Fig. 2a and b). These nanoparticles are stacked together, forming aggregates with a rough surface and abundant pores, which are favorable for providing a high specific surface area. The morphology of AgCl shows distinctly different characteristics (Fig. 2c and d). It consists of numerous fine dendritic structures interwoven into an open three-dimensional network resembling coral. This multi-branched morphology arises from ultrasound-induced anisotropic growth under non-equilibrium conditions. Cavitation generates localized extreme conditions and intense microjets that disrupt equilibrium cubic growth, promoting preferential growth along energetically favorable directions under diffusion-limited aggregation.[21,22] The AgCl/Malachite composite exhibits a sponge-like morphological feature, characterized by loosely packed nanoparticle agglomerates with rough surfaces and abundant interparticle voids (Fig. 2e and f). Such a hierarchical pore structure not only significantly increases the effective specific surface area of the material but also provides favorable channels for the mass transfer and diffusion of reactants and products, which is expected to enhance the interfacial reaction efficiency during photocatalytic processes. To further investigate the chemical composition and elemental distribution of the composite, energy-dispersive X-ray spectroscopy (EDS) elemental mapping was performed (Fig. 2g–k). The results indicate that the material consists of five elements: O, C, Ag, Cl, and Cu. The signals of all elements show a highly uniform spatial distribution across the scanned area. This confirms that under sonochemical synthesis conditions,

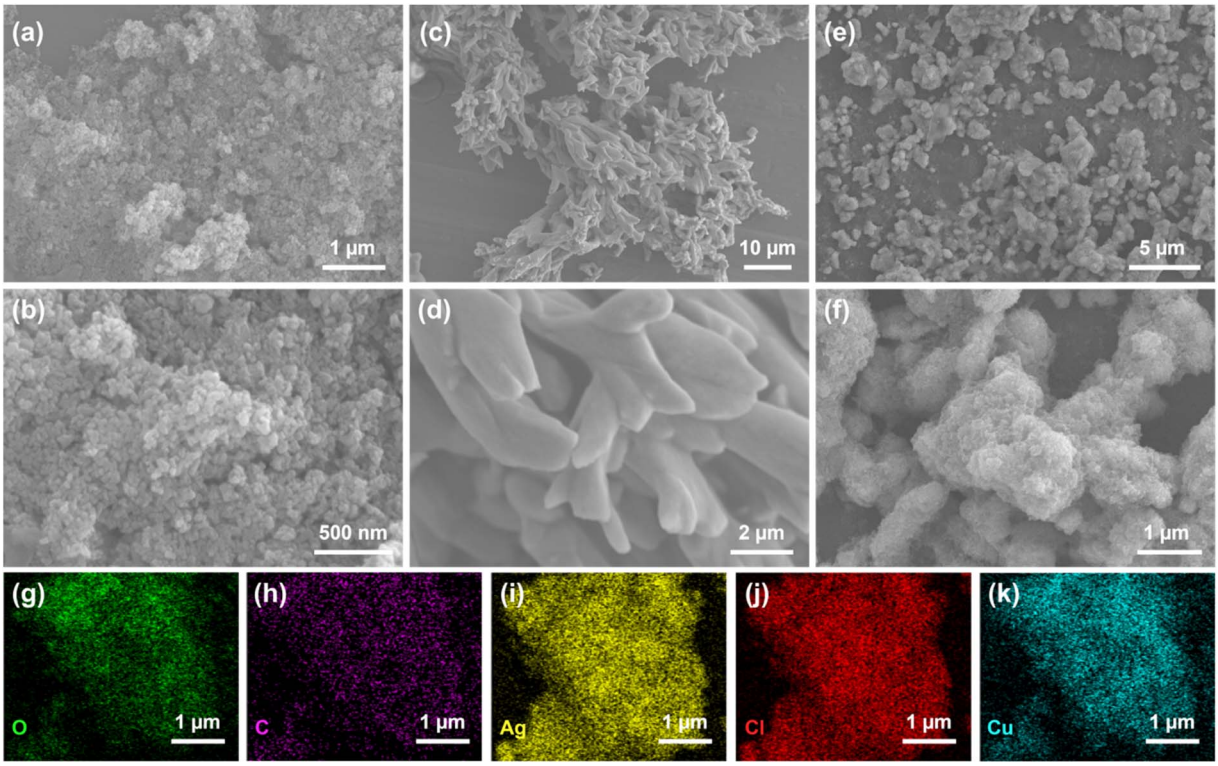


Fig. 2 SEM images of as-prepared samples, (a and b) Malachite; (c and d) AgCl and (e and f) AgCl/Malachite; elemental mappings of AgCl/Malachite: (g) O, (h) C, (i) Ag, (j) Cl, (k) Cu.

the two components, AgCl and Malachite, achieved uniform and intimate mixing at the nanoscale, rather than a simple physical blend. This homogeneous integration establishes a critical structural foundation for potential synergistic effects, such as efficient interfacial charge transfer, at the interface between the two phases.[23]

The textural properties of the catalysts, including specific surface area, pore volume, and pore size distribution, were characterized by $N_2$ physical adsorption analysis, with the results shown in Fig. 3. The adsorption–desorption isotherms of AgCl, Malachite, and the AgCl/Malachite composite all exhibit typical Type-IV curves accompanied by H3-type hysteresis loops[24–26] (Fig. 3a–c). This clearly confirms the presence of a predominantly mesoporous structure in all three materials. The pore size distribution curves, calculated from the desorption branch using the Barrett–Joyner–Halenda (BJH) model, further reveal differences in their pore characteristics. Pure-phase AgCl shows a relatively broad pore size distribution, indicating a network of larger interstitial pores (inset of Fig. 3a). In contrast, Malachite displays a more concentrated distribution, primarily within the smaller mesopore size range, suggesting a relatively uniform pore structure (inset of Fig. 3b). Notably, the pore size distribution of the AgCl/Malachite composite effectively integrates the features of both precursors (inset of Fig. 3c). The distribution curve exhibits a broader mesopore peak corresponding to AgCl, along with a contribution from the smaller pores originating from Malachite. This multi-scale composite pore structure, combining the transport channels provided by the mesopores of AgCl and the abundance of smaller pores contributed by Malachite, likely offers superior substrate mass transfer pathways and more interfacial active sites for catalytic reactions. This provides a structural explanation for the composite's significantly increased pore volume. The specific surface areas calculated using the Brunauer–Emmett–Teller (BET) equation are highly consistent with the aforementioned morphological and porosity analyses (Fig. 3d).

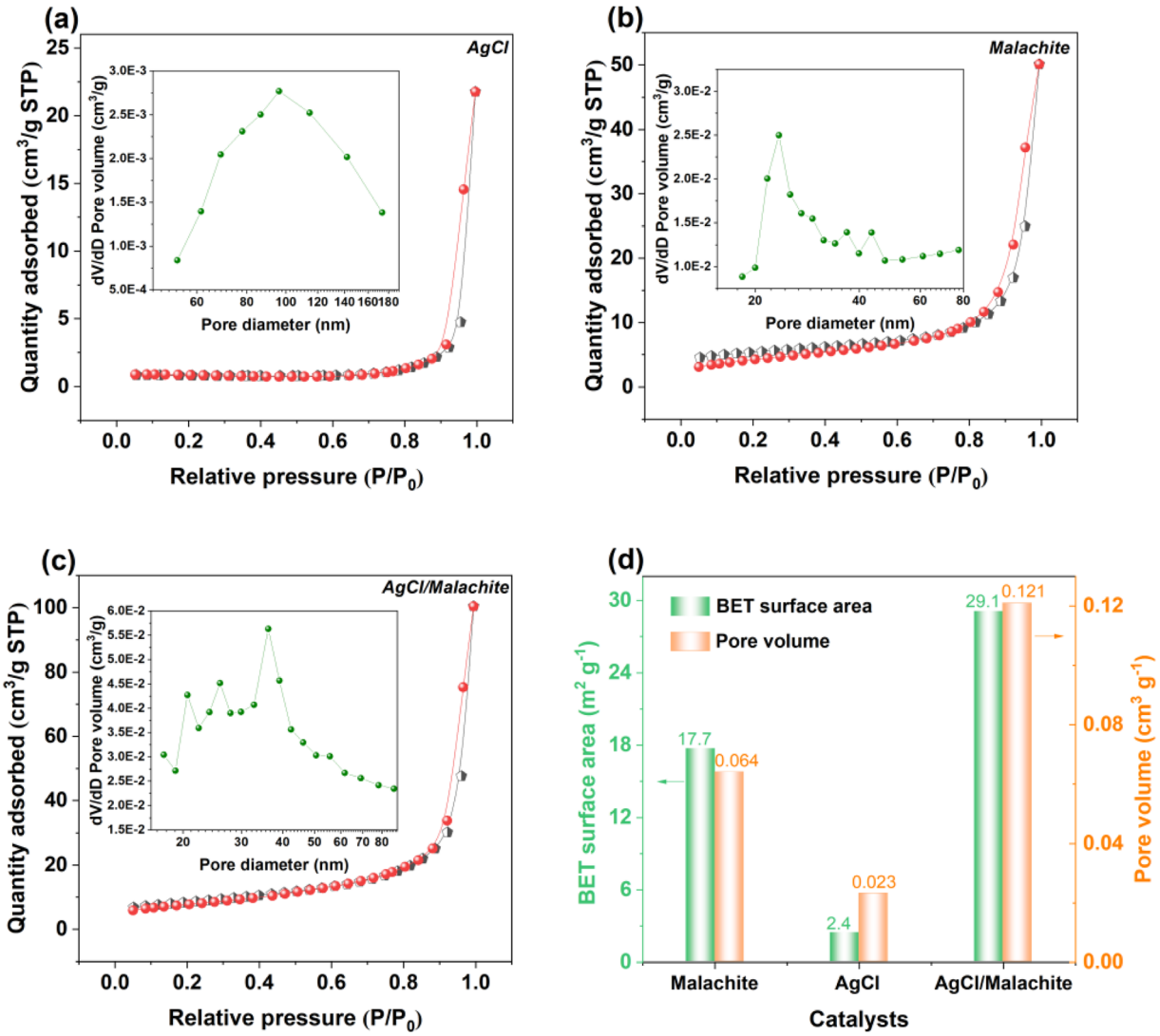


Fig. 3 $N_2$ adsorption–sorption isotherms and corresponding pore-size distribution curves (inset) for (a) AgCl; (b) Malachite and (c) AgCl/Malachite; (d) BET surface area and pore volume measurement results of AgCl, Malachite and AgCl/Malachite.

The dendritic, coral-like morphology of AgCl, despite its open structure, results in a relatively low specific surface area (2.4 $m^2$ $g^{-1}$) due to the larger dimensions of its branches. Pure-phase Malachite, formed by the agglomeration of nanoparticles, achieves a higher specific surface area (17.7 $m^2$ $g^{-1}$) attributed to the rough surface and pores created by particle stacking. In addition to the synergistic contribution from the hierarchical pore structure, the significant increase in specific surface area of the AgCl/Malachite composite (29.1 $m^2$ $g^{-1}$) compared to pure Malachite can be partly attributed to the sonochemical process. Ultrasonic cavitation effectively fragments Malachite particles, reducing their size and creating finer nanoparticles.[27] The loose packing of these refined particles generates additional interparticle voids, contributing to the enhanced surface area observed in the composite.[28] This material consists of densely agglomerated nanoparticles, forming a hierarchical macroscopic structure with an extremely rough surface and well-developed porosity. This ultimately results in a specific surface area and an abundance of hierarchical pore channels far exceeding those of the individual components. The increased specific surface area implies greater exposure of surface active sites, while the optimized multi-scale pore system facilitates reactant diffusion and mass transfer.[29,30] Their synergistic effect establishes a crucial physical structural foundation for enhancing the interfacial reaction efficiency of the material in photocatalysis.

The light absorption properties of the catalysts were characterized by ultraviolet-visible diffuse reflectance spectroscopy (UV-vis DRS). As shown in Fig. 4a. AgCl exhibits distinct absorption peaks at approximately 240 nm and 340 nm, attributed to its intrinsic UV light absorption. In the visible light region with wavelengths greater than 400 nm, AgCl displays a broad absorption band. This feature is often attributed to the localized surface plasmon resonance (LSPR) effect of trace $Ag^0$ nanoparticles.[31–33] In comparison, basic Malachite shows a strong absorption peak near 240 nm, followed by a decrease in absorbance. However, its absorption intensity increases again within the 500–700 nm range, which is related to its band structure as a visible-light-responsive semiconductor and possible d–d transitions.[34] Compared to pure Malachite, the AgCl/Malachite composite shows an overall decrease in light absorption intensity across the entire measured wavelength range. This decrease can be attributed to altered light scattering behavior at the interface following the formation of a heterojunction between AgCl and Malachite, thereby reducing the apparent absorbance signal collected during the diffuse reflectance measurement. Notably, the composite material exhibits enhanced light absorption compared to the single components at wavelengths greater than 480 nm, indicating superior photoresponsive capability in the visible to near-infrared region. This is beneficial for improving its catalytic performance under visible-light irradiation. The optical band gaps, calculated using the Tauc plot method ($(\alpha h\nu)^2$ *vs.* $h\nu$),[35,36] are presented in Fig. 4b. The band gaps of Malachite and AgCl are 3.11 eV and 2.97 eV, respectively. The band gap of the AgCl/Malachite composite slightly increases to 3.2 eV. The slight band gap increase of the composite is attributed to quantum confinement effects and local lattice strain at the heterojunction interface, which can subtly modify the electronic structure.[37] Although the direct light absorption capability of the composite is somewhat weakened, the effective coupling typically formed at the heterojunction interface might promote the separation and migration of photogenerated electron–hole pairs. This is expected to enhance quantum efficiency and, ultimately, improve its photocatalytic activity.

To investigate the photoelectrochemical properties and interfacial charge transfer kinetics of the materials, we performed transient photocurrent response (TPR) and electrochemical impedance spectroscopy (EIS) tests on the catalysts. As shown in Fig. 5a, under intermittent light illumination, the

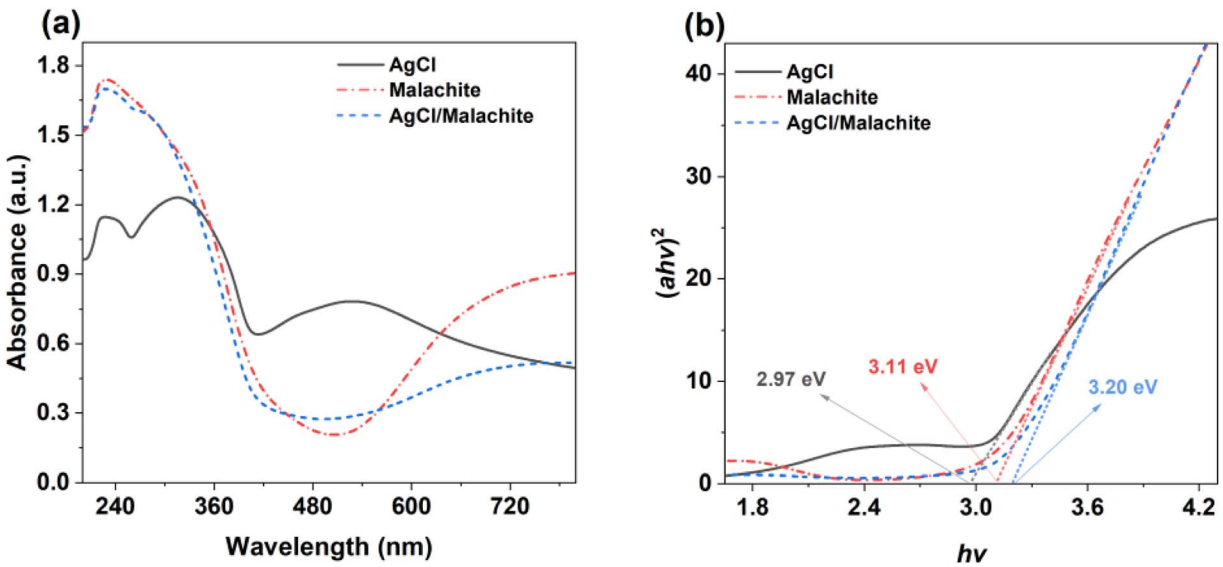


Fig. 4 Optical spectra of AgCl, Malachite and AgCl/Malachite, (a) UV-vis DRS, (b) $(\alpha h\nu)^2$ *versus* $h\nu$ for determining the optical band gap.

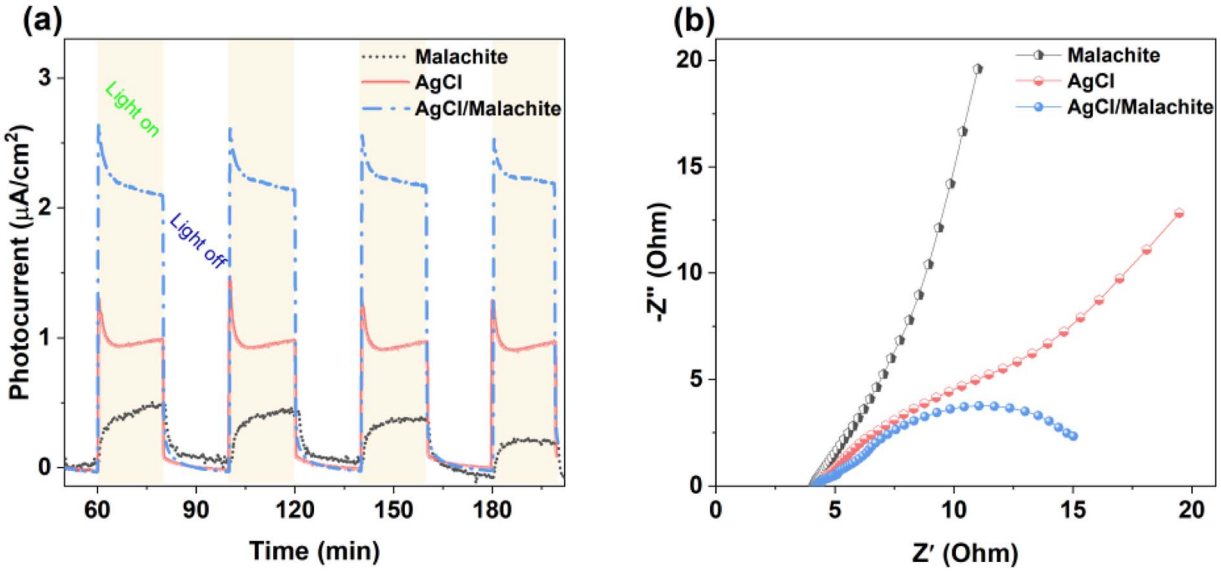


Fig. 5 Electrochemical test results of AgCl, Malachite and AgCl/Malachite, (a) transient photocurrent response; (b) Nyquist plots of electrochemical impedance spectroscopy.

AgCl/Malachite composite material exhibits a significantly enhanced and stable photocurrent response. After four on–off light cycles, its photocurrent density stabilizes at approximately 2.25 μA $cm^{-2}$, which is about 2.5 times and 10.2 times that of pure AgCl (0.92 μA $cm^{-2}$) and Malachite (0.22 μA $cm^{-2}$), respectively. The photocurrent density directly reflects the quantity of effective charge carriers generated under illumination and migrated to the external circuit.[38,39] The substantial increase in current density for the composite material clearly confirms that the heterojunction formed between AgCl and Malachite greatly enhances the separation efficiency and interfacial migration rate of photogenerated electron–hole pairs. This observation aligns with the aforementioned SEM and elemental distribution analyses: the uniform and intimate mixing of the two phases at the nanoscale provides ideal pathways for the efficient separation and rapid transport of photogenerated charge carriers at the interface, effectively suppressing bulk and surface recombination. The Nyquist plot obtained from EIS measurements further reveals the kinetic advantage in interfacial charge transfer (Fig. 5b). The diameter of the semicircle in the high-frequency region corresponds to the charge transfer resistance. The semicircle diameter for the AgCl/Malachite composite is significantly smaller than those of the two single components, indicating a lower charge transfer resistance.[40,41] The notable reduction in impedance is directly attributed to the built-in electric field (IEF) formed at the heterojunction interface. This field drives the directional migration of photogenerated electrons ($e^-$) and holes ($h^+$) in opposite directions, thereby substantially lowering the energy barrier required for charge transfer across the interface and accelerating the charge transfer process. This finding is consistent with the observed enhancement in carrier separation efficiency from the photocurrent tests. The PEC and EIS results corroborate each other, collectively revealing a core mechanism: the construction of an intimate heterojunction between AgCl and Malachite establishes efficient channels for charge separation and transfer at their interface. This is reflected not only in the significant increase in the number of photogenerated carriers but also in the substantial reduction of interfacial charge transfer resistance. Such optimized charge kinetic behavior provides a crucial kinetic foundation for the AgCl/Malachite composite material to achieve efficient and rapid pollutant mineralization in photocatalytic applications.

### 3.2. Photocatalytic activity evaluation of the catalysts

The photocatalytic activity of the catalysts was evaluated by degrading the model pollutant MO. As shown in Fig. 6a, during the 40 min dark adsorption phase, MO removal rates were measured as 5.5% for AgCl, 10.9% for Malachite, and only 1.0% for the AgCl/Malachite composite. The composite's notably low dark adsorption is primarily attributed to the intimate heterojunction formation between AgCl and Malachite, which prioritizes interfacial charge transfer over surface dye trapping.[42] Similar heterojunction systems have been reported to exhibit reduced dark adsorption due to the IEF directing charge carriers toward interfacial transfer rather than surface accumulation.[43] After 30 min of light irradiation, a blank control group without any catalyst showed only 5.8% self-degradation. In contrast, the introduction of catalysts significantly enhanced the degradation efficiency: pure-phase Malachite achieved a degradation rate of 16.7%, while AgCl with its dendritic coral-like morphology exhibited higher activity, reaching a degradation rate of 77.1% (Fig. 6b). This indicates that the AgCl prepared *via* the sonochemical method itself possesses good potential for photocatalytic MO degradation. The photocatalytic performance achieved a breakthrough enhancement upon combining AgCl with Malachite. When the atomic ratio of Ag to Cu in the composite was optimized to 1.2, the AgCl/Malachite sample

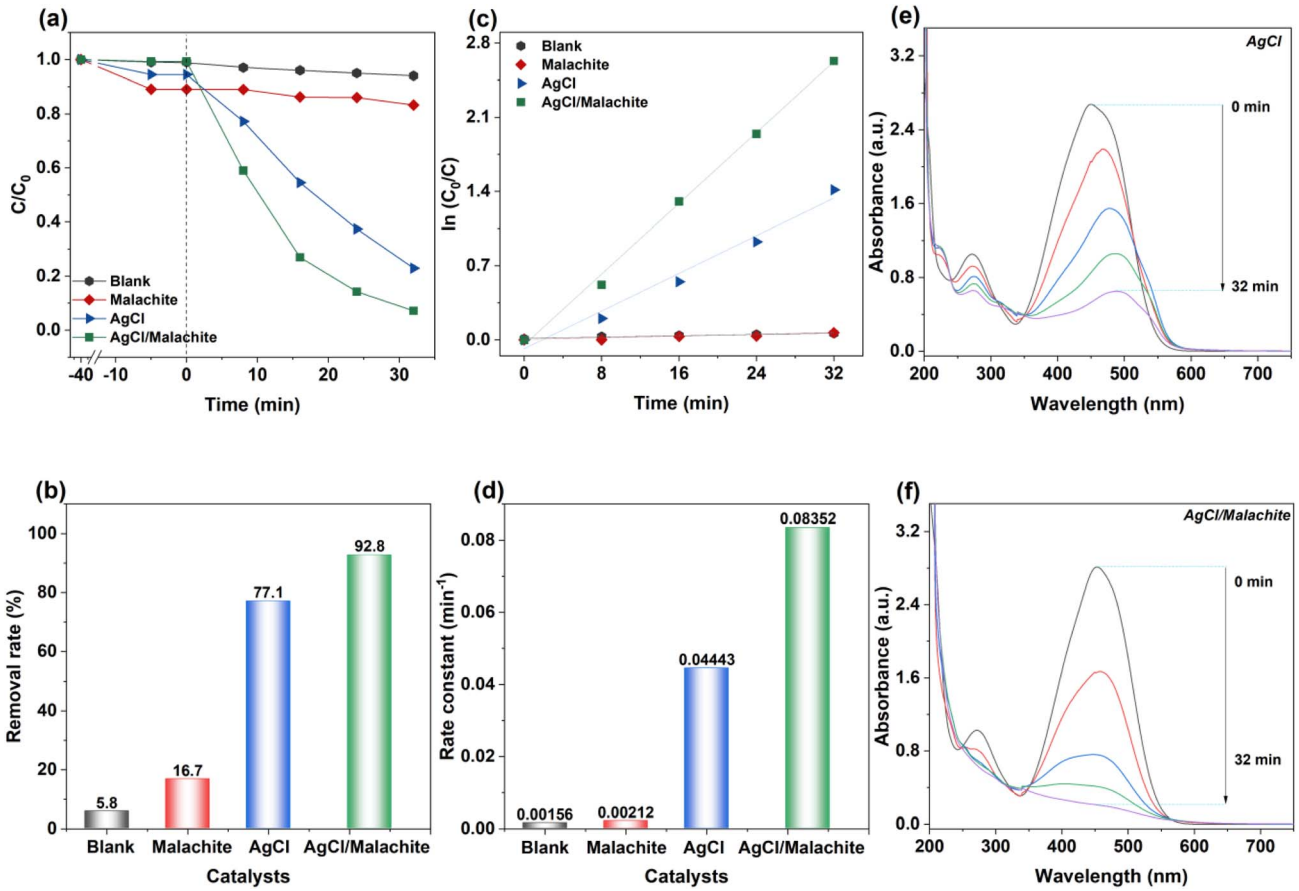


Fig. 6 (a) Photocatalytic performance of samples for MO degradation; (b) photocatalytic degradation rate of MO at 32 min illumination; (c) pseudo-first-order reaction kinetic curve of photocatalytic degradation of MO; (d) rate constant of photocatalytic degradation of MO; (e) UV-vis absorption spectra of MO with different reaction times over AgCl; (f) UV-visible absorption spectra of MO with different reaction times over AgCl/Malachite.

achieved a high MO degradation rate of 92.8% within 30 min (Fig. S1). This value represents an increase of 76.1% and 15.7% compared to pure Malachite and AgCl, respectively, indicating a significant synergistic catalytic effect arising from the composite formation, rather than a simple additive effect of the individual activities. To further quantify the reaction rates, the degradation process was fitted using a pseudo-first-order kinetic model ($-\ln(C/C_0) = k_t$), as shown in Fig. 6c. The apparent reaction rate constant for the AgCl/Malachite composite was as high as 0.08352 $min^{-1}$. As illustrated in Fig. 6d, this rate constant is 39.4 times that of pure-phase Malachite (0.00212 $min^{-1}$) and 1.9 times that of pure-phase AgCl (0.04443 $min^{-1}$). The significant difference in kinetic data quantitatively confirms the advantage of the composite in catalytic reaction kinetics, demonstrating an order-of-magnitude enhancement in reaction rate. Real-time monitoring of the MO degradation process *via* UV-vis absorption spectroscopy (Fig. 6e and f) provided direct evidence for the degradation mechanism. The characteristic absorption peak of MO molecules at ~460 nm originates from their azo chromophore group. Under the action of the AgCl/Malachite composite, the intensity of this characteristic peak decreased rapidly and continuously with irradiation time, at a rate much faster than that observed with single-component catalyst systems (Fig. S1). This phenomenon directly proves that the composite material can more effectively attack and destroy the chromophoric structure of MO molecules, thereby achieving rapid decolorization and mineralization of the dye.

The cyclic stability of a photocatalyst is a crucial indicator for its potential practical application. The photocatalytic stability of pure AgCl and the AgCl/Malachite composite was systematically evaluated through five consecutive cyclic degradation experiments, with the results presented in Fig. 7a. After five cycles, the photocatalytic performance of pure AgCl showed significant degradation, with its MO degradation rate sharply declining from an initial 71% to 40.8%. This decrease in activity can typically be attributed to that some $Ag^+$ ions in AgCl may be reduced by photogenerated $e^-$ to metallic silver, which deposits on the catalyst surface, leading to the coverage of active sites or inducing photocorrosion.[44,45] In stark contrast, the AgCl/Malachite composite exhibited exceptional cyclic stability. After five cycles, its degradation rate for MO remained above 90% (decreasing only slightly from 92.8% to 90.3%), with negligible activity loss. This result clearly demonstrates that

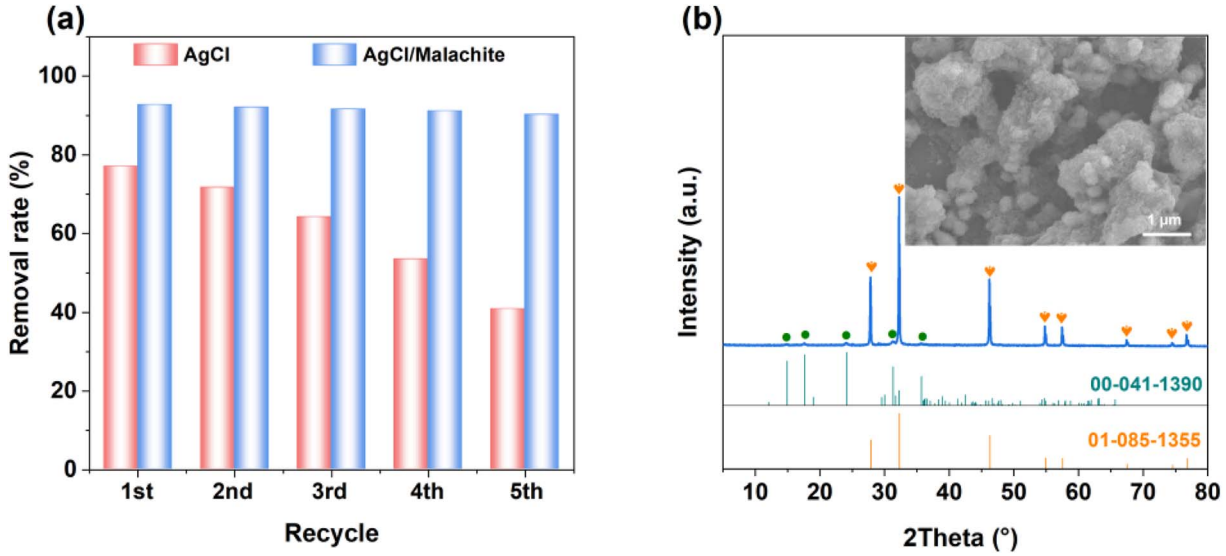


Fig. 7 (a) Stability test of AgCl/Malachite in the recycling reactions for MO removal; (b) XRD pattern and SEM image of AgCl/Malachite after photocatalytic tests.

compositing with Malachite effectively enhances the catalytic durability of the material. The AgCl/Malachite sample after cyclic use was further characterized by XRD and SEM (Fig. 7b). The XRD pattern showed no detectable diffraction peaks corresponding to metallic $Ag^0$ and no significant shifts in the main AgCl peaks, indicating that the crystalline integrity of AgCl was well preserved throughout the photoreaction. Consistently, SEM images further revealed that the characteristic sponge-like porous morphology of the material remained largely unchanged without observable structural collapse. The consistent preservation of crystal structure and morphology provides a coherent structural basis for the observed catalytic stability. In summary, the AgCl/Malachite composite not only demonstrates significantly enhanced initial photocatalytic activity but also possesses high cyclic stability, which is lacking in pure AgCl. Its stability originates from the effective suppression of photocorrosion in the AgCl component by the heterojunction structure, combined with its own robust hierarchical porous architecture. This combination of high efficiency and durability renders the prepared AgCl/Malachite composite a highly promising photocatalytic material with great potential for practical application, offering a viable candidate for sustainable dye wastewater treatment technologies.

### 3.3. Catalytic reaction mechanism

Based on systematic radical scavenging experiments and semiconductor band structure calculations, the reaction mechanism for the photocatalytic degradation of MO by the AgCl/Malachite composite material was investigated in depth. Key reactive species in the photocatalytic process were identified through quenching experiments using specific radical scavengers[46–48] (Fig. 8a). The experimental results indicate: upon addition of sodium carbonate ($Na_2CO_3$), a $h^+$ scavenger, the MO degradation rate drastically decreased by 49.4%, demonstrating that $h^+$ is the dominant active species. Adding isopropanol (IPA), a hydroxyl radical ($^{\bullet}OH$) scavenger, suppressed the degradation rate by 28.3%, indicating that $^{\bullet}OH$ is an important synergistic active species. After adding *p*-benzoquinone (BQ), a superoxide radical ($^{\bullet}O_2^-$) scavenger, the system still maintained a high degradation rate of 88.6%, confirming that $^{\bullet}O_2^-$ contributes minimally to the reaction. Thus, the photocatalytic system follows a synergistic mechanism involving $h^+$ and $^{\bullet}OH$, with $h^+$ playing the most critical role. The semiconductor band structure dictates the generation and migration behavior of photogenerated charge carriers. According to calculations using the Mulliken electronegativity formula:[49,50] the band gaps ($E_g$) of AgCl and Malachite, as determined by DRS, are 2.97 eV and 3.11 eV, respectively. The calculated valence band ($E_{VB}$) and conduction band ($E_{CB}$) potentials for AgCl are 3.06 eV and 0.09 eV, respectively. For Malachite, the valence and conduction band potentials are 3.72 eV and 0.61 eV, respectively. Based on the above band alignment, the charge transfer in the AgCl/Malachite heterojunction follows a *Z*-scheme mechanism (Fig. 8b). Under light irradiation, both components generate electron–hole pairs. The photogenerated $e^-$ from the conduction band of Malachite (0.61 eV) recombine with the $h^+$ from the valence band of AgCl (3.06 eV) at the intimately formed heterojunction interface. This interfacial recombination leaves $e^-$ in the AgCl conduction band (0.09 eV) and highly oxidative $h^+$ in the Malachite valence band (3.72 eV). This interfacial charge transfer, corroborated by photoelectrochemical and band structure analyses, enables efficient spatial charge separation that suppresses $e^-$–$h^+$ recombination.[51] The strongly oxidative $h^+$ enriched in the valence band of Malachite with sufficient thermodynamic driving force to directly oxidize MO and generate $^{\bullet}OH$ radicals from $H_2O/OH^-$.[52] The $e^-$ in the conduction band of AgCl, with a potential (0.09 eV) much more positive than the standard reduction potential of $O_2/^{\bullet}O_2^-$ (−0.33 eV), are thermodynamically unable to reduce $O_2$ to $^{\bullet}O_2^-$.[53,54] This

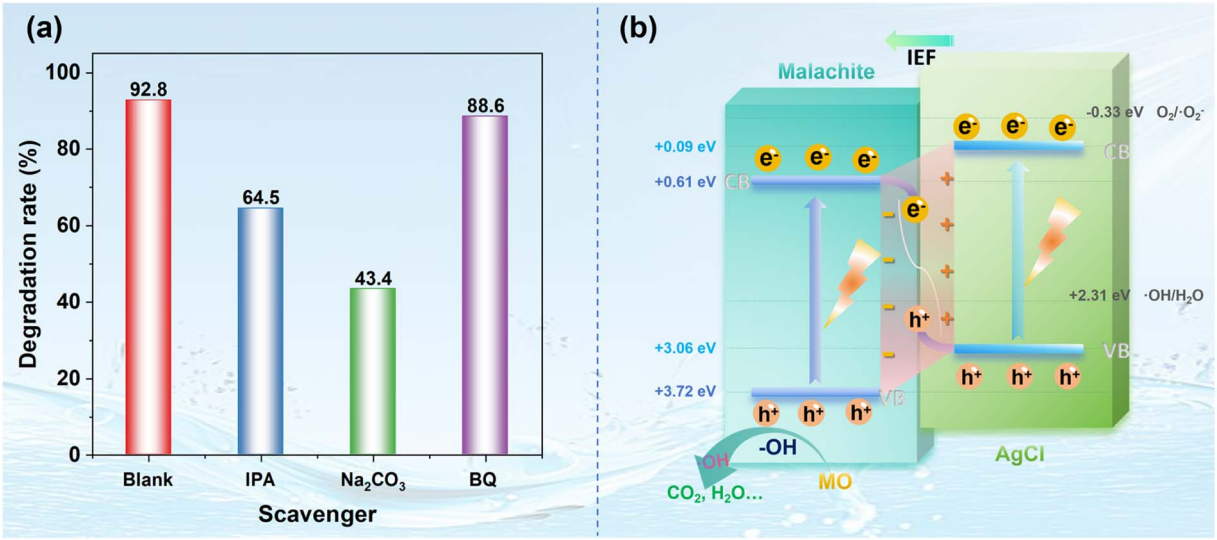


Fig. 8 (a) Effect of various scavengers on the degradation of MO over AgCl/Malachite; (b) photocatalytic mechanism of the AgCl/Malachite in MO degradation.

explains the minimal contribution of $^{\bullet}O_2^-$ observed in the quenching experiments. In summary, the superior photocatalytic performance of the AgCl/Malachite composite originates from the synergistic effect of the following multiple advantages: optimized charge kinetics: the IEF formed at the interface of the AgCl/Malachite heterojunction efficiently drives the spatial separation and directional migration of photogenerated $e^-$ and $h^+$, providing abundant $h^+$ and $^{\bullet}OH$ for the reaction. Favorable mass transfer and reaction interface: the sponge-like hierarchical porous structure and high specific surface area of AgCl/Malachite facilitate the rapid diffusion of reactant molecules and provide abundant active interfaces for the reactive species. Extended light utilization capability: the enhanced light absorption of the AgCl/Malachite composite in the visible region enables the generation of more photogenerated charge carriers.

## 4. Conclusion

This study successfully prepared a sponge-like porous AgCl/Malachite heterojunction *via* a sonochemical method. The composite exhibited exceptional photocatalytic activity. Under simulated light irradiation, it achieved a degradation rate of MO as high as 92.8% within 30 minutes. The rate constant (0.08352 $min^{-1}$) for MO photodegradation was 39.4 times that of pure-phase Malachite and 1.9 times that of pure AgCl, indicating a significant synergistic catalytic effect arising from the combination of AgCl and Malachite. Furthermore, the AgCl/Malachite composite demonstrated far superior cycling stability compared to pure AgCl, which is attributed to the effective suppression of photocorrosion of the AgCl component by the heterojunction structure. The excellent photocatalytic activity is attributed to optimized charge dynamics, favorable mass transfer and reaction interfaces, as well as enhanced light utilization capability. This work not only developed a novel photocatalytic material with both high-efficiency degradation capability and excellent stability for treating organic dye wastewater, but also elucidated the structural basis for its performance enhancement from a mechanistic perspective. The employed sonochemical method, characterized by its rapid and controllable nature, provides a reproducible and easily scalable synthetic paradigm for the controlled preparation of such heterojunction porous materials. This research offers new insights and a feasible technical pathway for developing next-generation, high-performance, and highly stable practical photocatalytic materials.

## Conflicts of interest

The authors declare no competing financial interest.

## Data availability

The data supporting the findings of this study are included within the article and its supplementary information (SI) files. Supplementary information: detailed experimental procedures, characterization, additional performance evaluation details, and figures. See DOI: https://doi.org/10.1039/d6ra01246a.

## Acknowledgements

This work was funded by the Key Project of the Education Department of Hunan Province (24A0610, 22A0581), the Natural Science Foundation of Hunan Province (2026JJ80621) and the Project of the College Student Innovation Training Program (S202510545042, 202510545009).

## References


1 H. Li, X. Liu, S. Wang and Z. Wang, *J. Environ. Manage.*, 2022, **315**, 115156.
2 N. Salehpour, P. Mahdavi and S. Nojavan, *Trends Environ. Anal. Chem.*, 2026, **49**, e00299.
3 P. Wang, A. Chen, H. Lian, S. M. Ahmadzai, F. Chang, Y. Pan, Y. Chen, B. Zhang, H. Zeng and C. Wei, *J. Environ. Chem. Eng.*, 2026, **14**, 121344.
4 W. Zhu, J. Chen, T. Xiao, Q. Qiu, L. Bi, K. Yang and T. Liang, *Environ. Res.*, 2026, **290**, 123436.
5 J. Wu, J. Xia, R. Gao, Z. Yi, K. Gong, K. Lu, W. Huang, C. Yu and K. Yang, *Chem. Eng. J.*, 2026, **527**, 171608.
6 Z. Zhu, X. Xing, Q. Qi, W. Shen, H. Wu, D. Li, B. Li, J. Liang, X. Tang, J. Zhao, H. Li and P. Huo, *Chin. J. Struct. Chem.*, 2023, **42**, 100194.
7 H. He, Z. Luo and C. Yu, *J. Alloys Compd.*, 2020, **816**, 152652.
8 C. L. Yu, H. B. He, X. Q. Liu, J. L. Zeng and Z. Liu, *Chin. J. Catal.*, 2019, **40**, 1212–1221.
9 J. Zhang, J. Wei, L. Yang, A. Cao, Z. Sun, Y. Yuanfeng, X. Shen, B. Chen and G. Chen, *Mol. Catal.*, 2026, **590**, 115667.
10 K. Zhang, A. Feng, C. Ou, Q. Wu, Z. Meng, H. Chen, S. Xu, X. Fu, W. Liao, B. Fang and G. Zhong, *Environ. Res.*, 2026, **293**, 123785.
11 Y. Quan, M. Feng, M. Liu, L. Dou, C. Ren and Z. Wang, *Appl. Surf. Sci.*, 2025, **708**, 163774.
12 J. Yang, F. Gao, X. Yu, J. Li, Y. Tang, Y. Tian and V. A. L. Roy, *Adv. Compos. Hybrid Mater.*, 2025, **8**, 417.
13 A. M. Abdel-Hafeez and M. A.-H. Abdel-Goad, *Discov. Sustain.*, 2025, **6**, 906.
14 B. Wang, C. Wang, Y. Tang, H. Yang, Y. Tian, X. Yu and Q. Li, *Appl. Surf. Sci.*, 2025, **697**, 162970.
15 H. He, J. Li, C. Yu and Z. Luo, *Sustainable Mater. Technol.*, 2019, **22**, e00127.
16 H. B. He, Z. Z. Luo and C. L. Yu, *Colloids Surf. A Physicochem. Eng. Asp.*, 2021, **613**, 126099.
17 W.-L. Ren, W.-J. Gao, Q. Zhou, J.-X. Jin and Y.-Q. Huang, *Inorg. Chem. Commun.*, 2024, **168**, 112919.
18 X. Ling, X. Guo, K. Wang, Z. Huang, Z. Mo, H. Qin, L. Duan, X. Meng and H. Wang, *Surf. Interfaces*, 2025, **72**, 107416.
19 Y. Zhao, Y. Song, S. Sun, S. Yao, L. Wang, W. Li and S. Li, *J. Water Proc. Eng.*, 2024, **59**, 105021.
20 J. Wang, M. Wang, Y. Wang, Z. Wei, X. He, H. Zang, X. Jin and L. Zhang, *Sci. China Chem.*, 2024, **68**, 1597–1607.
21 H. He, S. Xue, C. Yu and Q. Fan, *Chin. J. Inorg. Chem.*, 2016, **32**, 625–632.
22 C. Yu, H. He, W. Zhou, Z. Liu and L. Wei, *Sep. Purif. Technol.*, 2019, **217**, 137–146.
23 D. Meroni and C. L. Bianchi, *Curr. Opin. Green Sustainable Chem.*, 2022, **36**, 100639.
24 C. Wang, R. Yan, M. Cai, Y. Liu and S. Li, *Appl. Surf. Sci.*, 2023, **610**, 155346.
25 S. Xie, J. Jiang, G. Zhou, Y. Chen, A. Zhang, X. Xia, M. Shi, B. Deng, C. Yu and H. He, *Inorg. Chem. Commun.*, 2025, **173**, 113845.
26 B. Sumithra, V. Saravanan, C. Ramalingan, D. Sivaganesh, P. Lakshmanan and D. Geetha, *Tungsten*, 2024, **7**, 255–267.
27 T. A. Hassan, V. K. Rangari, R. K. Rana and S. Jeelani, *Ultrason. Sonochem.*, 2013, **20**, 1308–1315.
28 S. Sankar, N. Kaur, S. Lee and D. Y. Kim, *Ceram. Int.*, 2018, **44**, 8720–8724.
29 H. He, L. Zeng, X. Peng, Z. Liu, D. Wang, B. Yang, Z. Li, L. Lei, S. Wang and Y. Hou, *Chem. Eng. J.*, 2023, **451**, 138628.
30 H. He, J. Xiao, Z. Liu, B. Yang, D. Wang, X. Peng, L. Zeng, Z. Li, L. Lei, M. Qiu and Y. Hou, *Chem. Eng. J.*, 2023, **453**, 139751.
31 S. Fu, Z. Chu, Z. Huang, X. Dong, J. Bie, Z. Yang, H. Zhu, W. Pu, W. Wu and B. Liu, *RSC Adv.*, 2024, **14**, 3888–3899.
32 T. M. N. Bui, T. K. Vo, T. M. Quang, V. S. Nguyen, M. Q. Nguyen, T. Hung Le and T. H. Duc, *Colloids Surf. A Physicochem. Eng. Asp.*, 2025, **725**, 137626.
33 X. Li, Y. Guo and X. Feng, *Mater. Sci. Semicond. Process.*, 2025, **185**, 108900.
34 D. Chen, X. Wang, X. Zhang, W. Wang, Y. Xu, Y. Zhang and G. Qian, *Int. J. Hydrogen Energy*, 2020, **45**, 24697–24709.
35 H. Li, Z. Zhu, K. Yang, K. Lu, X. Chen, W. Huang and Z. Liu, *Environ. Sci.: Nano*, 2025, **12**, 1908–1921.
36 H. He, W. Peng, J. Jiang, X. Xia, J. Luo, S. Luo, X. Wang, K. Yang and C. Yu, *Colloids Surf. A Physicochem. Eng. Asp.*, 2025, **723**, 137420.
37 J. Thyr, J. Montero, L. Österlund and T. Edvinsson, *ACS Nanosci. Au*, 2021, **2**, 128–139.
38 S. Sun, C. Wang and S. Li, *Chin. J. Struct. Chem.*, 2024, **43**, 100398.
39 Y. Y. Yan, L. T. Du, M. R. Cao, N. Hu, L. J. Ye, J. H. Jiang, B. De, C. L. Yu and H. B. He, *J. Chin. Ceram. Soc.*, 2024, **52**, 133–142.
40 H. He, Y. Luo, Z. Luo and C. Yu, *Prog. Chem.*, 2019, **31**, 561–570.
41 H. He, S. Xue, Z. Wu, C. Yu, K. Yang, G. Peng, W. Zhou and D. Li, *Chin. J. Catal.*, 2016, **37**, 1841–1850.
42 C. Cheng, J. Zhang, B. Zhu, G. Liang, L. Zhang and J. Yu, *Angew. Chem., Int. Ed.*, 2023, **62**, e202218688.
43 T. Ali, Y. Li, B. Fang, S. Raza and Y. Xiao, *J. Mater. Chem. C*, 2026, **14**, 2721–2735.
44 F. D. Ali, S. H. Ammar, N. D. Ali, Y. R. Abdulmajeed and Z. H. Jabbar, *Mater. Sci. Semicond. Process.*, 2024, **172**, 108100.
45 Y. Shiraishi, Y. Hiroaki, S. Ichikawa, S. Tanaka and T. Hirai, *Chem. Commun*, 2025, **61**, 8496–8499.
46 T. Liu, H. Huang, Y. Liu, K. Papadikis, B. L. Mehdi, P.-S. Yap and G. Dawson, *J. Mol. Liq.*, 2024, **414**, 126026.
47 C. Yu, H. He, Q. Fan, W. Xie, Z. Liu and H. Ji, *Sci. Total Environ.*, 2019, **694**, 133727.
48 B. Zhang, X. Li, P. Liu, Q. Kong and W. Zhu, *J. Mater. Eng.*, 2024, **52**, 160–169.
49 H. He, S. Xue, Z. Wu, C. Yu, K. Yang, L. Zhu, W. Zhou and R. Liu, *J. Mater. Res.*, 2016, **31**, 2598–2607.
50 T. Yang, P. Deng, L. Wang, J. Hu, Q. Liu and H. Tang, *Chin. J. Struct. Chem.*, 2022, **41**, 2206023–2206030.
51 W.-y. Li, H. Yu, M. Yang, X. Dong, Y. Yang and T. Wang, *J. Alloys Compd.*, 2026, **1050**, 185691.

52 C. Chen, X. Zhu, H. Yu, M. Yang, X. Dong and Y. Yang, *Solid State Sci.*, 2025, **168**, 108025.
53 J. J. Samraj, R. Manju, M. Ashokkumar and B. Neppolian, *J. Clean. Prod.*, 2025, **492**, 144846.
54 C. Zhou, H. Yu, M. Yang, X.-t. Dong and Y. Yang, *ACS Appl. Nano Mater.*, 2025, **8**, 12828–12839.